

# Effects of the Crustal Magnetic Fields and Changes in the IMF Orientation on the Magnetosphere of Mars: MAVEN Observations and LatHyS Results.

N. Romanelli<sup>1</sup>, R. Modolo<sup>1</sup>, F. Leblanc<sup>2</sup>, J-Y. Chaufray<sup>1</sup>, S. Hess<sup>3</sup>, D. Brain<sup>4</sup>,  
J. Connerney<sup>5</sup>, J. Halekas<sup>6</sup>, J. McFadden<sup>7</sup>, B. Jakosky<sup>4</sup>.

Corresponding author: N. Romanelli, Laboratoire Atmosphere, Milieux et Observations Spatiales (LATMOS), IPSL, CNRS, UVSQ, UPMC, Tour 45-46, 4 place jussieu, 75252 Paris cedex 05, Paris, France. (Norberto.Romanelli@latmos.ipsl.fr) orcid.org/0000-0001-9210-0284

<sup>1</sup>Laboratoire Atmosphere, Milieux et Observations Spatiales (LATMOS), IPSL, CNRS, UVSQ, UPMC, Paris, France.

<sup>2</sup>LATMOS/IPSL, UPMC, Univ Paris06 Sorbonne Universités, UVSQ, CNRS, Paris, France.

<sup>3</sup>Office National d'Etudes et de Recherches Aérospatiales, Toulouse, France.

This article has been accepted for publication and undergone full peer review but has not been through the copyediting, typesetting, pagination and proofreading process, which may lead to differences between this version and the Version of Record. Please cite this article as doi: 10.1029/2017JA025155

**Abstract.** The Mars Atmosphere and Volatile Evolution Mission (MAVEN) is currently probing the complex Martian environment. Although main structures arising from the interaction between the solar wind (SW) and the induced magnetosphere of Mars can be described using a steady state picture, time-dependent physical processes modify the response of this obstacle. These processes result from temporal variabilities in the internal and/or external electromagnetic fields and plasma properties. Indeed, the crustal magnetic fields (CF) rotation constantly modifies the intrinsic magnetic field topology relative to the SW. Moreover, the magnetosphere's state is also modified by changes in the interplanetary magnetic field (IMF). In this work we analyze MAVEN magnetic field and plasma measurements obtained on 23 December 2014, between 06:00 UT - 14:15 UT. These measurements suggest

---

<sup>4</sup>Laboratory for Atmospheric and Space  
Physics, University of Colorado, Boulder,  
Colorado, USA.

<sup>5</sup>NASA Goddard Space Flight Center,  
Greenbelt, Maryland, USA.

<sup>6</sup>Department of Physics and Astronomy,  
University of Iowa, Iowa City, Iowa, USA

<sup>7</sup>Space Sciences Laboratory, University of  
California, Berkeley, California, USA.

the external conditions remained approximately constant when MAVEN was inside the magnetosphere during the first orbit. In contrast, MAVEN observed changes in the IMF orientation before visiting the magnetosphere during the second orbit. To investigate the response of the Martian plasma environment to the CF rotation and IMF variability, we also perform hybrid simulations, using MAVEN observations to set SW external conditions. Simulation results are compared with the MAVEN measurements and show good agreement. Associated recovery timescales of different magnetospheric regions are found to range between  $\sim 10$  s and  $\sim 10$  min. Finally, we do not observe large variability in the total planetary  $H^+$  and  $O^+$  escape rates at different times during this event, although a correlation between the latter and the CFs location is identified.

**Keypoints:**

- We study the responses of the Martian magnetosphere to variability in the IMF orientation, including crustal magnetic field effects.
- Estimated recovery timescales of different magnetospheric regions range between  $\sim 10$  s and  $\sim 10$  min.
- Computed  $H^+$  and  $O^+$  planetary ion loss rates do not show strong changes with the variability in the IMF orientation.

## 1. Introduction

Mars does not have a significant intrinsic global magnetic field [Acuña et al., 1998]. As a result, there is a direct interaction between the magnetized solar wind (SW) and the atmosphere of this planet. As part of this interaction, the atmosphere of Mars is subject to several ionizing mechanisms such as photo-ionization, charge-exchange and electron impact. Also, through several current systems [e.g., Baumjohann et al., 2010], it generates perturbations in the streaming interplanetary magnetic field (IMF), leading to its draping around the Martian ionosphere. In the locations where the collisionless regime holds, the IMF frozen into the plasma piles up around the stagnation region of the flow, and drapes around the body while the flow diverts around the object. While this process tends to create an induced magnetic tail formed by two lobes of opposite magnetic polarity separated by a current sheet, additional effects due to the presence of crustal magnetic fields (CF) [Acuña et al., 1999] give rise to a more complex magnetic field topology in this region. Such complexity has led to a large amount of observational studies on the properties and dynamics of the Martian magnetotail, based on various space missions [e.g., Yeroshenko et al., 1990; Dubinin et al., 1991; Luhmann et al., 1991; Vaisberg, 1992; Zhang et al., 1994; Lundin and Barabash, 2004; Romanelli et al., 2015; Luhmann et al., 2015; Dubinin and Fraenz, 2015; DiBraccio et al., 2015, 2017; Artemyev et al., 2017]. In addition, different theoretical approaches have been used to describe this particular plasma environment and, more generally, to determine magnetotail properties associated with nominal draping of the magnetic field lines [see, e.g., Chacko and Hassam, 1997; Ma et al., 2004; Modolo et al., 2012; Romanelli et al., 2014; Naor and Keshet, 2015].

Recent reviews on the plasma, magnetic field and atmospheric escape inside the induced magnetosphere (IM) of Mars, and upstream from the planetary bow shock (BS) can be found in Nagy et al. [2004]; Mazelle et al. [2004]; Bertucci et al. [2011]; Lillis et al. [2015]; Brain et al. [2017].

Despite that the main regions and boundaries resulting from the coupling between the SW plasma and the Martian magnetosphere can be described using a steady state picture, the response and state of this obstacle can be strongly modified by time-dependent processes. Indeed, the planetary neutral and plasma environment can be strongly affected by temporal variability in properties of the magnetized SW (i.e., bulk speed and mean ion density, IMF orientation and magnitude) and solar radiation fluxes, over different timescales. For instance, a seasonal dependence of the H exosphere has been recently observed by different spacecraft instruments [Chaffin et al., 2014; Clarke et al., 2014, 2017; Yamauchi et al., 2015; Bhattacharyya et al., 2015; Romanelli et al., 2016; Rahmati et al., 2017; Halekas et al., 2017; Halekas, 2017], with higher column densities generally observed near Martian perihelion and lower column densities near aphelion. The solar wind dynamic pressure has been found to affect the location and shape of the magnetospheric boundaries (bow shock, magnetic pile-up) [Edberg et al., 2009] and the heavy ion planetary escape rates [Edberg et al., 2010]. By means of hybrid numerical simulations, Modolo et al. [2012] have shown that changes in the IMF direction also affect the orientation of the bow shock and the magnetic pile-up boundary, the location of the oxygen plume [Dong et al., 2015] and the magnetic field topology inside the Martian magnetosphere, with different timescales. Several studies have also identified effects that crustal magnetic fields have on the solar wind interaction with Mars, the magnetospheric boundaries location and

the atmospheric loss [e.g., Ma et al., 2014, 2015; Brecht and Ledvina, 2014; Fang et al., 2015, 2017]. Remnant crustal magnetic fields on Mars rotate with the planet and thus they constantly alter the magnetic field configuration interacting with the solar wind, at a period of 24 h 37 min. Moreover, Futaana et al. [2008], Dubinin et al. [2009] and Jakosky et al. [2015a] have shown that solar extreme events (corotating interaction regions and coronal mass ejections) are capable of increasing the atmospheric planetary escape rate in a factor that varies between 10 and 100, compared to nominal solar wind conditions. A time-dependent MHD model has also been used to quantify the impact of a strong coronal mass ejection on the Martian magnetosphere [Ma et al., 2017]. Indeed, the authors have shown that the plasma environment around Mars changes rapidly due to the disturbances in the solar wind and that ion escape rates increase by more than one order of magnitude during this event.

In spite of the progress in the understanding of this space plasma environment, studies on the responses of the Martian induced magnetosphere to SW variations are still needed. This is due to the large amount of non-linear time-dependent physical processes taking place in such interaction, the proper limitations of (spatially and temporally) localized spacecraft observations and instrumental design (e.g., field of view, sampling frequency, range of mass and energy of the instruments), and the computationally expensive time-dependent numerical simulation calculations. To enhance our current knowledge of this coupled system, we seek to study the outcomes of the Martian environment to variability in each of the external parameters, separately. In this work, we perform an analysis of the temporal evolution of the Martian magnetosphere to changes in the IMF direction, taking into account the rotation of crustal magnetic fields. More specifically, we analyze

Mars Atmosphere and Volatile Evolution (MAVEN) [Jakosky et al., 2015b] plasma and magnetic field measurements during an eight hours time interval, approximately. This time interval has been chosen given its potential for studying the Martian magnetosphere state during stable external conditions and after observed variability in the IMF orientation. To provide a comprehensive framework to help to interpret such in situ observations and to determine global properties (recovery timescales, ion loss rates) of the magnetosphere of Mars subject to those external conditions, we also perform several Hybrid Simulation LatHyS [Modolo et al., 2016] stationary and dynamical runs. Given the particular complexity of the Martian magnetotail, we study characteristics of the near tail magnetosheath (MSH) and tail lobes in more detail.

The present study is structured as follows. In Section 2 we briefly describe the capabilities of the MAVEN Magnetometer (MAG), Solar Wind Ion Analyzer (SWIA) and Supra-Thermal And Thermal Ion Composition (STATIC) instruments and the LatHyS model. In Section 3 we present and analyze MAG and SWIA observations during the time interval under study. In Section 4 we perform a comparison between LatHyS simulation results and MAVEN data, and we provide estimations for the recovery timescales of different regions inside the Martian magnetosphere. Estimations of the planetary proton and oxygen ion loss rates are also computed. A discussion of the results is developed in Section 5, and our conclusions are presented in Section 6.

## 2. Description of MAVEN Instruments and LatHyS Numerical Simulation

### Model

#### 2.1. The MAVEN Magnetometer (MAG)

The MAG instrument is designed to provide vector magnetic field measurements around Mars with two independent fluxgate magnetometers placed on extended solar array panels. Both magnetometers possess a broad range (to 65,536 nT per axis), an intrinsic sampling frequency of 32 Hz and accuracy of 0.25 nT. A detailed description of this instrument can be found in Connerney et al. [2015]. In this work we have used full time resolution MAG data.

#### 2.2. The MAVEN Solar Wind Ion Analyzer (SWIA)

SWIA is an energy and angular ion spectrometer covering an energy range between 25 eV/q to 25 keV/q (with 48 logarithmically spaced energy steps) with a field of view (FOV) of  $360^\circ \times 90^\circ$  [Halekas et al., 2015]. The energy and intrinsic time resolution of SWIA are 14.5% and 4 s, respectively. SWIA observes towards the solar wind direction most of the time, although it also observes the nadir direction around periapsis. In this work we used the measured energy ion flux spectra, and the derived mean plasma density and bulk velocity (from the coarse 3d distribution) with 8 s resolution.

#### 2.3. Supra-Thermal And Thermal Ion Composition (STATIC)

STATIC is an energy, mass, and angular ion spectrometer, operating in the range of 0.1 eV/q to 30 keV/q (energy resolution between 11 and 16%), with a FOV of  $360^\circ \times 90^\circ$  (with  $22.5^\circ$  resolution) and a mass range from 1 to 70 amu [McFadden et al., 2015]. In this study we have used derived densities for  $H^+$  (from the d1 product) with 16 s resolution.

## 2.4. The LATMOS Hybrid Simulation (LatHyS) Model

LatHyS is a global three-dimensional multispecies hybrid model that allows to describe plasma processes taking place in several space plasma environments [Modolo et al., 2005, 2006, 2012, 2016, 2018]. It has been used to study the interaction between the solar wind and Mercury [Richer et al., 2012], the interaction between the Jovian plasma and Ganymede [Leclercq et al., 2016], the interaction between a magnetic cloud and a terrestrial magnetosphere [Turc et al., 2015] and the interaction between a coronal mass ejection and Mars [Romanelli et al., 2018].

LatHyS treats ion species kinetically. When applied to the Martian environment, it considers six ion species: solar wind  $H_{sw}^+$  and  $He_{sw}^{++}$ , and planetary  $H^+$ ,  $O^+$ ,  $O_2^+$ , and  $CO_2^+$ . The electrons are described by means of two massless fluids with different temperatures (solar wind and ionospheric) that ensure the quasi-neutrality condition. The solar wind electron population is assumed to be adiabatic, and the ionospheric electron population is modeled by a polytropic equation whose index varies between 0 and 5/3, depending on the electron density. The planetary/satellite ions are the result of three ionization processes acting on the obstacle's neutral envelope: photoionization, charge exchange, and electron impact. More generally, the local production rate of each ion species is computed from an assumed neutral environment (H, O and  $CO_2$  for Mars) and the self-consistent dynamics of the ions by considering model cross sections and ionization frequencies. The implementation of the crustal magnetic fields rotation at Mars is performed taking into account the model shown in Cain et al. [2003]. A detailed description of the LatHyS model can be found in Modolo et al. [2016] and references therein. A review of the hybrid and

other formalisms used to model different plasma environments can be found in Winske et al. [2003]; Ledvina et al. [2008]; Kallio et al. [2011].

In this work we perform numerical simulations with 80 km spatial resolution and 0.0617 s time step (i.e., 0.0333 times the background proton cyclotron gyro-period). The simulation for the complete studied event required 465000 timesteps and considered approximately  $4.42 \times 10^8$  macroparticles. It was performed on the Calcul Intensif for Climate, Atmosphere and Dynamic (CICLAD) server, and required about 2000 h on 256 CPUs (0.5 millions of CPU hours). The simulation domain extends from  $-2.4$  to  $2.4 R_M$  in  $X_{MSO}$  axis and from  $-4.5$  to  $4.5 R_M$  in  $Y_{MSO}$  and  $Z_{MSO}$  axes ( $R_M$  stands for Martian radii,  $1 R_M = 3393$  km). The Mars Solar Orbital (MSO) coordinate system is centered at Mars and is defined as follows: the X axis points toward the Sun, the Z axis is perpendicular to Mars's orbital plane and is positive toward the ecliptic north. The Y axis completes the right-handed system. External conditions for the simulation runs are set using MAVEN measurements during the time interval under consideration. Given that the orbital velocity of MAVEN around Mars is on the order of 5 km/s, simulated profiles (magnetic field, mean plasma velocity, plasma density) along MAVEN's trajectory have a temporal resolution on the order of 15 s. We describe the Martian neutral environment by one-dimensional radial density profiles for  $\text{CO}_2$ , O and H, assuming spherical symmetry. This allow us to study effects on the Martian magnetosphere and planetary ion loss rates that are unequivocally associated with variabilities in the IMF orientation and the crustal magnetic field rotation, rather than due to asymmetries in the Martian atmosphere and exosphere. In the case of  $\text{CO}_2$  and O, they are a combination of five exponential terms, with reference densities and scale heights shown in Modolo et al. [2016] (see values considered for RUN B in Table 1 of

that work). In the case of H, we assume two isothermal populations in pressure equilibrium under the gravity field of Mars (Equation 13 in Modolo et al. [2016]). Reference densities and lengths for these two populations are  $1.5 \exp(5) \text{ cm}^{-3}$ , 25965 km and  $1.9 \exp(4) \text{ cm}^{-3}$ , 10365 km.

### 3. MAVEN Observations on 23 December 2014 06:00 - 14:15 UT

Figure 1 displays magnetic field and plasma data obtained by MAVEN MAG, SWIA and STATIC instruments as a function of time, during two orbits on 23 December 2014, between 06:00 and 14:15 UT. From top to bottom, this Figure shows the energy per charge spectra of the ion flux measured by SWIA, the associated mean plasma velocity in MSO coordinates, ion densities derived from both STATIC and SWIA, and the magnetic field data (in MSO). During the time interval under study, MAVEN is initially located in the pristine SW. The mean IMF between 06:45-07:15 UT is  $\mathbf{B}_1 = [0.29 \pm 0.59, -5.55 \pm 0.23, -0.99 \pm 0.51] \text{ nT}$ , where the ranges are the standard deviation in each component. After crossing the bow shock (around 07:17 UT), MAVEN enters into the Martian MSH measuring stronger wave activity, higher magnetic field intensity, plasma compression and smaller plasma bulk velocity. Except during the 08:00:00 - 08:14:30 UT time interval (studied in more detail later), the observed values of the  $B_{XMSO}$  component in the MSH and magnetotail are compatible with nominal draping of the IMF (with the major component along the  $-\mathbf{Y}_{MSO}$  axis). After entering the nominal wake, MAVEN reaches closest approach at 08:43 UT at an altitude of  $\sim 150$  km close to the Northern pole. MAVEN then enters again into the MSH and goes back to the SW, crossing the BS around 09:20 UT. MAVEN displays no signatures of changes in the IMF orientation (with respect to the  $\mathbf{B}_1$ ), at least inside the Martian MSH. The mean

IMF between 09:36 - 10:06 UT is  $\mathbf{B}_2 = [0.88 \pm 0.52, -5.26 \pm 0.30, -1.32 \pm 0.78]$  nT, basically equal to  $\mathbf{B}_1$  taking into account the standard deviations during both time intervals.

Moreover, the SW bulk velocity and density corresponding to both times intervals are

$\mathbf{U}_1 = [-295 \pm 3, 29 \pm 2, 35 \pm 5]$  km/s and  $\mathbf{U}_2 = [-301 \pm 2, 29 \pm 3, 12 \pm 6]$  km/s, and

$n_1 = (10.6 \pm 0.4)$  cm<sup>-3</sup> and  $n_2 = (11.5 \pm 0.5)$  cm<sup>-3</sup>, respectively. The derived values for

each of these parameters upstream from the Martian bow shock are very close between

each-other, and the associated standard deviation is relatively small. This therefore sug-

gest that the external conditions remained approximately constant when MAVEN was

inside the Martian magnetosphere. Among variabilities in the internal conditions, the

rotation of the crustal fields must be taken into account. The subsolar GEO latitude dur-

ing this time interval is  $-24.6^\circ$  (Mars was close to the Southern Summer Solstice) while

the subsolar GEO longitude (ssl) varies between  $157^\circ$  at 07:00 UT and  $132^\circ$  at 08:43 UT.

The strongest crustal field region is concentrated around  $180^\circ$  GEO longitude. Therefore,

for instance, in the cases of ssl= $0^\circ$  and ssl= $180^\circ$  the strongest crustal fields are on the

nightside and dayside, respectively. It is also worth pointing out that the anomalous in-

crease in the SWIA mean velocity taking place between 08:00 UT and 08:04 UT arises

from computation techniques disregarding the presence of  $O^+$  and  $O_2^+$  ions in the plasma.

Changes in the orientation of the IMF are observed before MAVEN crosses the BS

again, around 11:50 UT. For instance, the IMF components varied rapidly at 10:47 UT,

performing a rotation (mainly) in the plane perpendicular to the  $X_{MSO}$  axis. The IMF

intensity does not change significantly during this event. Another fast variability in the

IMF orientation occurred at 11:17 UT, followed by a slower reorientation of the  $Y_{MSO}$

and  $Z_{MSO}$  IMF components. In contrast with this, SW velocity and density values do not

differ significantly from the ones already estimated during the previous orbit. When inside the Martian magnetosphere, MAVEN traverses the same regions as before, finding again a magnetic field configuration consistent with the mean IMF observed right before the BS crossing and with the one between 14:00 and 14:15 UT. Also consistent with the observed changes in the IMF orientation, MAVEN clearly observes the plume of O<sup>+</sup> planetary ions during the inbound leg of the first orbit (first panel), while it is not detected during the second one.

The trajectory of MAVEN on 23 December 2014 between 06:00 and 14:15 UT is displayed (brown curve) in cylindrical MSO coordinates in Figure 2. Color-coded points display MAVEN's position every 15 minutes. Figure 2 also shows the average location of the BS (in black) and the magnetic pile-up boundary (in blue), based on the fit by Vignes et al. [2000]. The initial position of MAVEN is marked by the blue dot closest to the black arrow. As can be seen, the inbound BS crossings took place at one of the flanks (close to the terminator plane) while the outbound crossings are close to the nose. This explains the different time intervals spent by MAVEN in the MSH during the inbound and outbound legs.

## 4. Numerical Simulation Results and Comparison with MAVEN data

### 4.1. The Martian IM before the first observed IMF rotation

As shown in the previous section, observations suggest that the external conditions are constant during the first studied orbit. We perform numerical simulations to model the Martian magnetosphere and to determine signatures associated with crustal magnetic fields along MAVEN's trajectory, during this time interval. The external conditions considered for these simulations are:  $\langle \mathbf{B} \rangle = \frac{\mathbf{B}_1 + \mathbf{B}_2}{2}$ ,  $\langle n \rangle = \frac{n_1 + n_2}{2}$  and

$\langle \mathbf{U} \rangle = \left( \frac{\mathbf{U}_1 + \mathbf{U}_2}{2} \right)_{X_{MSO}} \hat{X}_{MSO}$ . We fix the plasma beta of solar wind  $\text{H}_{sw}^+$ ,  $\text{He}_{sw}^{++}$  and electrons at 0.93, 0.19 and 1.50, respectively, for nominal SW temperatures. Figure 3 shows the magnetic field as a function of time (along MAVEN's trajectory) derived from the LatHyS code. From top to bottom, this Figure shows the corresponding Bx, By, Bz MSO components and the magnetic field magnitude. The blue and green curves in each panel are derived from stationary simulated states obtained for the planetary subsolar longitude at 07:00 UT (MAVEN upstream from the Martian BS) and at CA, respectively. The red curve is constructed taking a linear interpolation between 12 magnetospheric states (snapshots) obtained during a dynamical simulation (varying ssl), as follows:

$$B_i(t) \equiv B_i^{t_j} \left[ 1 - \frac{t - t_j}{\Delta t_j} \right] + B_i^{t_{j+1}} \left[ \frac{t - t_j}{\Delta t_j} \right] \quad (1)$$

where  $B_i^{t_j}$  is the magnetic field  $i$  component along MAVEN's trajectory predicted by LatHyS at snapshot time  $t_j$ , and  $\Delta t_j$  is the time interval between two consecutive snapshots. MAVEN MAG measurements are also shown in black, for easy comparison. As can be seen in Figure 3, there is general good agreement between the simulations results and MAVEN MAG data, mainly for altitudes higher than 400 km (where proper limitations of the Cain model [Cain et al., 2003] interpolated into the Cartesian grid are reduced). Draping of the IMF is well reproduced in both direction and magnitude during the majority of the studied event. Numerical simulations do not reproduce the Bx component between 08:00 and 08:14:30 UT where a change of sign is observed and difficult to interpret with a stationary picture of magnetic field draping, suggesting magnetotail flapping in absence of IMF variabilities [DiBraccio et al., 2015, 2017]. The main difference at high altitudes concerns the predicted bow shock location, particularly during the flank bow shock cross-

ing. Such difference can be partly due to the atmospheric profile considered for these simulation runs. These results suggest that the atmosphere might be denser than computed from the assumed one-dimensional radial profiles, contributing to a BS with larger cross section area around the terminator plane than simulated. Another factor involves long-term temporal variabilities of the heaviest ion planetary species densities ( $\text{CO}_2^+$  and  $\text{O}_2^+$ ). Indeed, when comparing different snapshots taken during the dynamical simulation, the bow shock cross section area generally increases when such densities increase. We also find good agreement between MAVEN observations and simulated profiles of the mean plasma velocity and total ion density, as can be seen in Figure 4. Analogous formula to Equation 1 is used to compute the dynamical simulation profiles for  $\mathbf{U}$  and  $n$ . Consistent with the hypothesis of an atmosphere denser than modeled, simulation results show a more pronounced transition of the mean plasma velocity between the magnetosheath and the induced magnetosphere than observed by MAVEN (during the inbound bow shock crossing). Indeed, a denser atmosphere would also increase the mass loading effect, creating a smoother variation of the bulk plasma velocity between the magnetosheath and the magnetotail boundary. Differences between simulation density profiles and MAVEN observations at low altitudes are likely due to low energy heavy planetary ion populations, not detectable in SWIA energy range. It is also interesting to notice that LatHyS simulations are also capable of reproducing very well the ion energy spectra observed by MAVEN along its trajectory. The solar wind ( $\text{H}_{sw}^+$  and  $\text{He}_{sw}^{++}$  ions), the  $\text{O}^+$  plume, the bow shock and magnetosheath are clearly identifiable in Figure 5. Same as before, given a reduction of the mass loading effect, we notice that the variation of the bulk velocity between the magnetosheath and the induced magnetosphere takes place more abruptly

that seen by SWIA (Figure 1, top panel). A comparison of the stationary and the dynamical simulation profiles for the magnetic field and plasma bulk velocity and density suggests that the effects of crustal magnetic fields (at least along MAVEN's trajectory) are mainly restricted to low altitudes ( $< 400$  km). Indeed, the simulated curves of each magnetic field component, mean plasma velocity and total ion density are very similar during almost all the studied event, when outside this altitude range.

#### 4.2. The Martian IMF: Rotation of the Martian Crustal Fields and the IMF

MAVEN MAG observations show changes in the IMF orientation taking place mainly in the Y-Z MSO plane, after 10:47 UT. Having determined signatures of crustal field effects on MAVEN measurements along the previous orbit, we perform dynamical simulation runs taking into account both the rotation of the crustal fields and the observed IMF variability. To do the latter, we have used MAVEN MAG  $B_{y_{MSO}}$  and  $B_{z_{MSO}}$  data between 10:47 and 14:00 UT as input for the IMF entering the simulation box. This IMF is afterward convected by the SW through the simulation domain. The  $X_{MSO}$  component of the IMF is kept constant and equal to the value considered in the previous section. Given that MAVEN is inside the Martian magnetosphere between 12:00 and 14:00 UT, the IMF during this time interval is derived from a linear interpolation between MAG measurements between these times. Figure 6 shows the dynamical LatHyS results (in red), and the corresponding MAVEN MAG and SWIA (in black) and STATIC (in green) data. From top to bottom, the  $B_x$ ,  $B_y$ ,  $B_z$  MSO components, the magnetic field magnitude  $|\mathbf{B}|$ , the  $U_x$ ,  $U_y$ ,  $U_z$ , MSO components, the bulk velocity magnitude  $|\mathbf{U}|$  and the mean ion density are shown. As can be seen, there is a good agreement between observations and simulations. The MSH and magnetotail are well reproduced, together with the draping

of the IMF and the corresponding variabilities in the mean plasma velocity and density.

The main differences are the ones already pointed out in the previous section: a mismatch between predicted and observed bow shock crossings, and a difference between observed and modeled crustal fields at low altitudes.

Thanks to the inclusion of the crustal fields rotation and the IMF temporal variability in the LatHyS code, together with the capability to reproduce the main signatures observed along MAVEN's trajectory, we can study the dynamical evolution of the Martian magnetosphere in more detail. To do this we make use of 105 snapshots derived from the dynamical simulation run. These snapshots, each of them displaying a magnetospheric state, are not separated by the same time interval. Instead, they are computed more frequently during time periods when the largest IMF variations seen by MAVEN take place.

We focus this analysis in the Martian magnetosheath (downstream from Mars) and the Martian magnetotail. The employed methodology is presented schematically in Figure 7.

We consider four planes perpendicular to the  $X_{MSO}$  axis, between  $X_{MSO} = -1.38 R_M$  and  $X_{MSO} = -2.38 R_M$ , separated by  $1/3 R_M$ , as shown in the right panel. For each of these planes, we consider four circular regions centered on  $Y_{MSO} = Z_{MSO} = 0 R_M$  (see left panel). The radial interval of these regions are the following:  $r=[0 - 1] R_M$ ,  $r=[1 - 1.75] R_M$ ,  $r=[1.75 - 2.5] R_M$  and  $r=[2.5 - 3.25] R_M$ . These regions are shown by the red circle, and the light blue, yellow and green rings, respectively. For each of these regions, we determine the centers of intensity  $\langle \mathbf{r} \rangle_+$  and  $\langle \mathbf{r} \rangle_-$  of the  $Bx_{MSO} > 0$  and  $Bx_{MSO} < 0$  magnetotail lobes. That is, we compute:

$$\langle \mathbf{r} \rangle_+ = \frac{\sum \mathbf{r}_{Y-Z} Bx_{MSO}(\mathbf{r}_{Y-Z})}{\sum Bx_{MSO}(\mathbf{r}_{Y-Z})}, \text{ for all } Bx_{MSO} > 0 \quad (2)$$

$$\langle \mathbf{r} \rangle_- = \frac{\sum \mathbf{r}_{Y-Z} Bx_{MSO}(\mathbf{r}_{Y-Z})}{\sum Bx_{MSO}(\mathbf{r}_{Y-Z})}, \text{ for all } Bx_{MSO} < 0 \quad (3)$$

where the sum in these calculations are performed for all position  $\mathbf{r}_{Y-Z}$  inside the region and plane of interest. Based on the two centers of intensity, we define a unitary vector (going from  $\langle \mathbf{r} \rangle_+$  to  $\langle \mathbf{r} \rangle_-$ ) that is used as a proxy to characterize the orientation of the corresponding magnetotail region. Additionally, we perform an estimate of the normal to the current sheet (in each of these planes) by means of a linear fit of all the locations with  $|\mathbf{r}_{Y-Z}| < 1 R_M$  where  $|Bx_{MSO}| < 0.5 \text{ nT}$ . Such linear fit and the normal to the current sheet are shown schematically by the orange straight line and vector, respectively.

An example of the determination of these points, superimposed to the local state of the Martian magnetosphere (magnetic field) in the plane  $X = -2.38 R_M$ , is shown in Figure 8. This figure displays the  $Bx_{MSO}$  component (color-coded) as a function of  $Y_{MSO}$  and  $Z_{MSO}$  coordinates. Black arrows correspond to the local magnetic field component perpendicular to the  $X_{MSO}$  axis. The left panel displays a magnetotail cross section when it is close to a quasi-stationary state (simulated profile at time =10:14:27 UT), while a non-equilibrium configuration is clearly observed in the right panel (time =10:48:40 UT). Each pair of green, yellow, light blue and red crosses (encircled to facilitate identification) correspond to the centers of intensity determined for the positive and negatives lobes in each of the 4 circular regions, from the most external to the inner one, respectively. Locations close to the current sheet with  $|Bx_{MSO}| < 0.5 \text{ nT}$  are shown in grey. The orange straight line corresponds to the associated linear fit, and the derived current sheet normal is shown with the orange vector. For easy comparison, the orientation of the mean IMF (at this plane) upstream from the bow shock is also shown (together with the normal plane) by the thick black vector (and black straight line) centered at (0,0). As can be seen in the

left panel, the (thick) orange and black vectors are almost over-imposed, showing that the inner magnetotail is well adapted to the local IMF at this time. Moreover, the vectors going from  $\langle \mathbf{r} \rangle_+$  to  $\langle \mathbf{r} \rangle_-$  for each region (crosses with the same colors) are close to be parallel to these two vectors. In contrast with this, the right panel shows that the (thick) black and orange vectors have very different orientations. Moreover, the vector going from  $\langle \mathbf{r} \rangle_+$  to  $\langle \mathbf{r} \rangle_-$  for the external region (green crosses) is close to the IMF orientation of this plane while the ones for the inner regions (the red and blue light ones) are close to the orange vector. The location of the yellow crosses point toward an intermediate state, between the IMF and the nominal wake configurations. To quantify the relative orientation between different structures inside the magnetotail and magnetosheath, we define the angle  $\theta$  between a vector in the Y- $Z_{MSO}$  plane and the  $Z_{MSO}$  axis (varying from  $-180^\circ$  to  $180^\circ$ ). In the case of  $\mathbf{B}_\perp$  (perpendicular to the  $X_{MSO}$  axis),  $\theta = -101.4^\circ$  and  $\theta = -34.2^\circ$  for the left and right panels, respectively. The corresponding angle  $\theta$  between the computed vectors of each region and the  $Z_{MSO}$  axis are the following. For the left panel, from the tail magnetosheath to inner lobes,  $\theta$  is equal to  $-102.3^\circ$  (green),  $-102.4^\circ$  (yellow),  $-101.8^\circ$  (light blue),  $-106.5^\circ$  (red) and  $-102.6^\circ$  (orange, based on the linear fit). For the right panel, the values of  $\theta$  (in the same order) are:  $-35^\circ$  (green),  $-83^\circ$  (yellow),  $-102.5^\circ$  (light blue),  $-100.3^\circ$  (red) and  $-100.2^\circ$  (orange).

To study the temporal variability of the Martian magnetotail and magnetosheath, we estimate these angular variables for the four planes and for the 105 snapshots derived from the dynamical simulation. The upper panel in Figure 9 shows the set of angular variables evaluated at the plane  $X = -2.38 R_M$ , as a function of time. A highly similar behaviour is observed at the other three planes. The bottom panels show the values of the angular

variables for the four planes as a function of time, during the two time intervals when the strongest changes in the IMF orientation take place. As can be seen, the main difference between curves related to the same region (same color) is a time shift. This is the result of the time required for a perturbation to be convected by the local plasma from one plane to the other. In other words, we see a highly similar reaction of each region inside the magnetotail, for  $Y_{MSO} - Z_{MSO}$  planes between  $X_{MSO} = -1.38R_M$  and  $X_{MSO} = -2.38R_M$ . Moreover, it is clear that the external circular region (magnetosheath) adapts very quickly and is capable of following the IMF rotation, after a small time delay (difference in the convection time of the plasma upstream and in the MSH). With regard to the inner lobes, we see that they follow the change in the IMF orientation in a smoother way and with a much larger time delay. This is due to the magnetic field line diffusion across the Martian ionosphere. We can also clearly see the transition in the adaptation of the Martian magnetosphere to changes in the IMF orientation, between the magnetosheath and the inner magnetotail (yellow curves).

Based on the derived values for  $\theta$ , we compute angular velocities by means of linear fits for each of the regions. This fitting is performed during time intervals displaying signatures of adaptation to rotations of the IMF. The results are shown in Table 1. From left to right, the columns of this table show the region under analysis, the corresponding computed angular velocity, the time interval under which the linear fit is performed, the  $R^2$  value and number of points associated with such a fit, and the ratio between the derived angular velocity in this region and that of the IMF rotation we associate to this behaviour. This table displays the results related to the three time intervals with the fastest IMF rotations detected by MAVEN. As expected, the rotation of the magnetotail

and magnetosheath take place in the same sense as that of  $\mathbf{B}_\perp$ . Two of these cases concern changes where  $|d\theta/dt|$  for  $\mathbf{B}_\perp$  (IMF) is positive (20.6°/min and 97.1°/min), and the third one takes place in the opposite sense (−36.2°/min). The absolute value of the angular velocity for each of the considered regions increases from the nominal wake towards the magnetosheath, for the three IMF rotation case study. For instance,  $|d\theta/dt|$  ranges approximately between 2°/min and 6°/min when considering the inner magnetotail, while it ranges between 20°/min and 84°/min when considering the external region. It is also interesting to notice the presence of a trend in the computed ratios, when considering each region separately. Indeed, these values are found to generally decrease for increasing IMF rotation angular velocities, therefore suggesting a limit for the recovery angular velocities of each region. Further, these results allow to estimate recovery timescales under such changing external conditions. For instance, in the case with the fastest IMF angular rotation, the recovery timescale of the inner magnetotail lobes is approximately 12 minutes, while the tail magnetosheath adapts in approximately 8 seconds.

### 4.3. Planetary $\text{H}^+$ and $\text{O}^+$ escape

The upper panel of Figure 10 shows the total  $\text{H}^+$  and  $\text{O}^+$  planetary escape rates as a function of time, derived from LatHyS runs. It also shows the escape rates through the plane  $X = -2.4 R_M$  for both ion species, and the  $\text{O}^+$  escape rate along the convective electric field direction. As can be seen, there is not a strong variability of these fluxes, particularly in the case of planetary protons. As shown in Table 2, the mean  $\text{H}^+$  total escape is  $7.56 \times 10^{25}$  ion/s and the standard deviation during all the analyzed event is only 2% of this value. Also, 78% of the mean  $\text{H}^+$  total escape takes place across the  $X = -2.4 R_M$  plane, while the remaining 22% is approximately evenly distributed along directions

perpendicular to the  $X_{MSO}$  axis, with a small preference along the convective electric field direction. The mean  $O^+$  total escape is  $1.14 \times 10^{24}$  ions/s, with a standard deviation of the order of 7%. In this case, around 88% and 10% of the mean total escaping flux take place across the  $X = -2.4 R_M$  plane and the plane perpendicular to the convective electric field, respectively. Figure 10 (upper panel) also suggests that crustal magnetic fields can have an effect on the total  $O^+$  escape flux. As can be seen, the  $O^+$  loss rate displays a small variation with time, taking lower values ( $\sim 0.95 \times 10^{24}$  ions/s) between 07:30-08:30 UT (ssl between  $150^\circ$  and  $135^\circ$ ) and larger ones ( $\sim 1.15 \times 10^{24}$  ions/s) between 11:00-12:00 UT (ssl varying between  $98.6^\circ$  and  $84^\circ$ ). These results suggest that the  $O^+$  escape rate is anticorrelated with the strength of the crustal fields near the subsolar region, with a time delay around 2h 30 m (ssl is  $180^\circ$  at 05:25 UT). The lower panels display the  $O^+$  escape rates (total, through the plane  $X = -2.4 R_M$ , and along the convective electric field direction) and the value of  $\theta$  for the  $\mathbf{B}_\perp$  component of the IMF at the terminator plane as a function of time, for the two time intervals when the strongest changes in the IMF orientation take place. As shown in the lower left panel, changes in the computed  $O^+$  escape rates take place on approximately the same timescales than that of the IMF orientation during this time interval, with a small time delay. We do not observe the same variability for the computed  $O^+$  escape rates in the lower right panel. This difference is likely due to the smaller number of considered simulation snapshots and the smaller IMF rotation angular velocities that are observed during the latter time interval. Despite of this difference, mean values and standard deviations computed for the derived  $O^+$  escape rates during both time intervals are close to the corresponding values obtained during the rest of the (approximately 8 hours) analyzed event. It is worth mentioning that  $O_2^+$  and

$\text{CO}_2^+$  escape rates are not presented in this paper, since changes in the considered spatial resolution might affect the description of physical processes occurring in the ionosphere. Indeed, Modolo et al. [2016] analyzed the effects of such changes on LatHyS runs (up to 50 km) might have on the magnetospheric boundaries geometry and location and planetary escape rates. Even though they did not find significant changes in the computed  $\text{O}^+$  loss rates when considering 50 km and 80 km resolution simulations (under the same conditions), such conclusion is probably not fulfilled in the cases of  $\text{O}_2^+$  and  $\text{CO}_2^+$  heavier planetary species.

## 5. Discussion

Previous studies have shown that the interaction between the magnetized solar wind and the Martian magnetosphere is highly complex and time dependent. Given this complexity, we seek to improve our current understanding of this coupled system by studying the responses of the planetary plasma environment to changes in each of the external parameters, separately. In this work we focus our analysis on the responses of the magnetosphere of Mars to changes in the IMF orientation, including the rotation of crustal magnetic fields. We first study magnetic field and plasma measurements provided by MAVEN MAG, SWIA and STATIC on 23 December 2014, between 06:00 and 14:15 UT. The analysis of this data suggests that the external conditions remained approximately constant when MAVEN is inside the magnetosphere for the first time. However, MAVEN observes changes in the IMF orientation (without strong variabilities in the other external parameters) before visiting the magnetosphere for the second time. These conditions (stable external parameters during one orbit, variability solely in one of them during the second orbit) are not frequently observed by MAVEN, therefore this event constitutes an

excellent candidate for the purposes of this study. To help to interpret MAVEN data during this event and to determine global properties of the plasma environment around Mars under these conditions, we also perform LatHyS stationary and dynamical runs.

We find a general good agreement between the simulation results along MAVEN's trajectory and MAVEN MAG, SWIA and STATIC observations during these two orbits. In general, measurements and simulations results are consistent with nominal IMF draping around the Martian ionosphere, showing related deceleration, compression and heating of the SW plasma in the Martian MSH, as well as planetary escape rate occurring mainly through the induced magnetotail. Observations of the oxygen plume [Dong et al., 2015] in MAVEN SWIA data are also reproduced by LatHyS code. Among the differences, we find that the simulated bow shock cross section at the terminator plane is underestimated. This difference is likely due to the atmospheric profiles assumed for the simulation runs and effects deriving from temporal variability of the heavy planetary ion species production. Differences between MAVEN MAG observations and LatHyS simulations at altitudes  $< 400$  km are likely related to the proper limitations of the Cain model [Cain et al., 2003] and deviations due to the interpolation of this model into a Cartesian grid (spatial resolution 80 km). Differences between the Cain model and the computed interpolation into the LatHyS spatial grid are reduced around relatively large scale crustal magnetic fields, mainly located in the Southern hemisphere.

MAVEN observations between 08:00 and 08:14:30 UT show a magnetic field orientation that can not be explained in terms of nominal draping of the IMF, considering stationary external conditions during this time interval. During this approximately 15 minutes event, MAVEN's  $Y_{MSO}$  ranges between  $1.14 R_M$  and  $0.83 R_M$ ,  $Z_{MSO}$  ranges between  $-1.19 R_M$

and  $-0.57 R_M$  and  $X_{MSO}$  varies between  $-0.87 R_M$  and  $-1.15 R_M$ . These observations are therefore obtained inside and right next to the nominal magnetic pile up boundary, as also evidenced by the large  $B_{XMSO}$  values and the reduction of the  $B_{YMSO}$  component. Fluctuations in all magnetic field components have smaller amplitude compared to the ones observed in the MSH and have also been observed at these locations during other orbits (e.g., orbit 433, between Dec 19, 2014 20:00 UT and Dec 20, 2014 00:00 UT, not shown in this work). In principle, one could argue that the observed difference in the  $B_{XMSO}$  polarity during this event and the rest of MAVEN's magnetotail crossing could result from a rotation of the IMF. However, no signatures of such rotation are observed in MAG data inside the MSH (e.g., change in the local  $B_{YMSO}$  component). If such rotation would have taken place very close to the time MAVEN is crossing the magnetic pile-up boundary then, according to our simulation results, the inner magnetotail as a whole would not have enough time to adapt. These two arguments make unlikely to explain these measurements in terms of an IMF rotation and, since the model considers effects derived from crustal magnetic fields, we conclude that the observed polarity change in the tail lobe is likely due to flapping (steady or kink) of the neutral current sheet. Similar signatures have been recently reported and studied based on MAVEN data [DiBraccio et al., 2015, 2017]. Indeed, multiple current sheet crossings are often observed on any given orbit as MAVEN crosses the Martian magnetotail, under stable IMF conditions. Moreover, by applying the technique presented in Rong et al. [2015], DiBraccio et al. [2015, 2017] properly determined what kind of flapping was taking place for 30 identified set of current sheet crossing events fulfilling the latter condition. A necessary condition to use this technique is that MAVEN observes (at least) three complete current sheet

crossings, as it passes through the magnetotail. Unfortunately, this is not the case for the time interval under consideration in our study, preventing from further analysis.

We have also determined the recovery time scales of the magnetosheath and the magnetotail lobes at different distances downstream from Mars, between  $X_{MSO} = -1.38 R_M$  and  $X_{MSO} = -2.38 R_M$ . A firm understanding of the magnetic field dynamics in these regions can improve our current knowledge of several associated plasma acceleration processes and the resulting atmospheric escape rates. We do not find a significant difference between estimations associated with the same region (in the Y-Z MSO plane), for different  $X_{MSO}$  values. Moreover, while the external region of the magnetosheath adapts very quickly to IMF variabilities, the reconfiguration demands longer time intervals when considering regions closer to the nominal wake. Our results suggest that, under the external conditions explored in this study, recovery timescales of the inner magnetotail lobes can be estimated based on an angular velocity being of the order of 10% of that of the IMF rotation or less. This therefore suggests that in the case of an IMF rotation of  $180^\circ/\text{min}$  (lasting 1 minute), the recovery timescales of the magnetotail lobes in the nominal wake are in the order of 10 minutes or larger. As a result of the Martian ionosphere, the magnetic lobes follow IMF rotations through much smoother variations. In contrast with this, magnetic field draping adaptation in the magnetosheath takes place significantly faster, with recovery timescales that in such a case would be on the order of 10 seconds or less. Modolo et al. [2012] presented a study on the response of the Martian magnetosphere to a rotational magnetic field discontinuity. The larger simulation box, the lower spatial resolution (300 km), together with the focus on the dynamical evolution of the tail at locations separated by  $\sim 2 R_M$  provide complementary information. Interestingly, we find similar results regarding

the bow shock and magnetosheath properties and adaptation timescales. Differences are restricted to the computed recovery timescales of the inner magnetotail lobes, and are likely associated with the different solar wind parameter values and atmospheric profiles considered in each work.

The computed total planetary  $H^+$  and  $O^+$  escape rates do not display strong variabilities as a function of time, during the analyzed event. Under the studied internal and external conditions, mean values for these quantities are  $7.56 \times 10^{25}$  ions/s,  $1.14 \times 10^{24}$  ions/s, respectively. We find that the major part of these ions are escaping through the  $X_{MSO} = -2.4 R_M$  plane, and that around 10% of the total  $O^+$  escape takes place along the convective electric field. The computed total H ion loss rate is approximately twice the one reported in Modolo et al. [2005], under solar minimum conditions. The derived total O ion loss rate is close to the one reported in Dong et al. [2015] although, in that work based on MAVEN data, the authors focused only on ions with energies higher than 25 eV. Heavy ion escape rate in the same energy range was analyzed in Brain et al. [2015] and was found to exceed  $2 \times 10^{24}$  ions/s. Mean values and standard deviations of the  $O^+$  escape rates (total, through the plane  $X = -2.4 R_M$ , and along the convective electric field direction) during the two time intervals with the strongest changes in the IMF orientation are close to the corresponding values computed for the rest of the analyzed event. These results suggest that variability in the IMF orientation do not strongly affect the planetary  $O^+$  loss rates. We also notice that  $O^+$  loss rates vary slowly with the planetary subsolar longitude, approximately anticorrelating with the intensity of the dayside crustal field source, with approximately a 2h 30 m time delay. Similar values and trend have been reported in Ma et al. [2014], under solar minimum conditions, and for subsolar latitude

-13°. A longer LatHyS run to confirm the presence of this trend over a complete planetary rotation will be performed in a future study. Additional influences of crustal fields on the bow shock and magnetic pile-up boundary location present in our simulations might be masked by several factors: effects from temporal variabilities of the heavy ion planetary production rates (when external conditions are fixed), and the adaptation of these (non axi-symmetric) boundaries to changes in the IMF orientation. Finally, it is worth emphasizing the importance of complementary studies on the configuration and response of the Venusian magnetosphere to different IMF orientations and to its variability. Indeed, such analyses can improve our current understanding on the time-dependent interaction between induced magnetospheres and the SW under varying IMF configurations [e.g., Zhang et al., 2009; Masunaga et al., 2013; Vech et al., 2016]. Regarding the latter point, Masunaga et al. [2013] found that the total O<sup>+</sup> escape rate (integrated on the night-side) does not change significantly when comparing sets of events under quasi-parallel and quasi-perpendicular IMF (with respect to the SW direction). On the other hand, Vech et al. [2016] studied the effects of heliospheric current sheet crossings on the induced magnetosphere of Venus. Particularly, they found a reduction of the heavy ion flux in the near-Venus magnetotail after the passage of such IMF sector boundary crossings, possibly an outcome of the magnetic disconnection of the plasma tail from the planetary ionosphere associated with magnetic reconnection. Recent studies on magnetic reconnection in the Martian magnetotail can be found in Harada et al. [2015, 2017], based on MAVEN plasma and magnetic field measurements. In particular, one of the main conclusions of the latter study is that reconnection could be present around 1-10% of the time in this region. Given that MAVEN might have not measured reconnection structures taking place far

from the particular MAVEN orbit, such estimates should be considered as a very conservative minimum occurrence rate. Even though this shows that magnetic reconnection is an important process for the particle transport and rearrangement of the magnetic field topology in the Martian magnetotail, the associated consequences for the total planetary ion escape losses still require future additional statistical analysis of plasma and magnetic field observations and global numerical simulations results. However, it is worth pointing out that an auxiliary simulation (with a larger simulation box,  $X$  ending at the  $-5.73 R_M$  plane) using the fix external conditions seen by MAVEN during the first orbit does not present significant differences when compared to the one presented in this work (simulation box ending at the  $X = -2.4 R_M$  plane). In particular we do not find significant differences in the modeled magnetic field topology when comparing these two simulation runs.

## 6. Conclusions

Several works have shown that time-dependent interaction processes play a significant role and can modify the response of the Martian magnetosphere to the incoming solar wind [e.g., Edberg et al., 2010; Futaana et al., 2008; Dubinin et al., 2009; Jakosky et al., 2015a]. In this study we have analyzed MAVEN MAG, SWIA and STATIC data and performed numerical LatHyS runs to improve our understanding on the response of the Martian magnetosphere to changes in the IMF cross-flow component, including the rotation of the crustal fields. For the conditions of the studied event we find that the bow shock and magnetosheath adapt in the scale of seconds to the changes in the IMF direction. In contrast with this, the near magnetotail (between  $X_{MSO} = -1.38$  and  $-2.38 R_M$ ) recovery time scales vary depending on the region considered inside of it and take

values up to 10 times the typical time interval over which the IMF rotates. Moreover, the smoothness of the magnetospheric response also displays a trend: a sharper transition is observed in the magnetosheath, compared to the inner tail lobes. We do not find strong variabilities in the total  $H^+$  and  $O^+$  escape rates with time, although we observe an appreciable anticorrelation (with some time delay) between the crustal magnetic field intensity at the dayside of Mars and magnitude of the latter.  $O^+$  loss rates are not strongly affected by the observed changes in the IMF direction. In summary, this study presents key outcomes arising from time-dependent internal and external parameters and stresses the need to analyze spacecraft observations carefully, despite the agreement between steady-state pictures of the Martian plasma environment and results derived from statistical studies. Future studies will be focused on the influence of temporal variabilities in the solar wind bulk velocity and mean plasma density on different regions inside the Martian induced magnetosphere.

**Acknowledgments.** N.R. is supported by a CDD contract from Laboratoires d'excellence Exploration Spatiale des Environnements Planétaires (LABEX-ESEP ANR N° 2011-LABX-030). N.R. is also indebted to the French Space Agency CNES for its support. N.R., R.M., F.L. and J-Y.C. are indebted to CNRS for its support on the LIA MAGNETO and to ANR for the project TEMPETE (ANR-17-CE31-0016). This work is also part of HELIOSARES Project (ANR-09-BLAN-0223) and ANR MARMITE-CNRS (ANR-13-BS05-0012-02). Authors also acknowledge the support of the IPSL data center CICLAD for providing us access to their computing resources. MAVEN data are publicly available through the Planetary Data System (<https://pds-ppi.igpp.ucla.edu/>). Numerical simulations outputs used in this article can be found in <http://impex.latmos.ipsl.fr>.

## References

- Acuña, M. H., et al. (1998), Magnetic field and plasma observations at Mars: Initial results of the Mars Global Surveyor mission, *Science*, 279 (5357), 1676-1680.
- Acuña, M. H., et al. (1999), Global distribution of crustal magnetization discovered by the Mars Global Surveyor MAG/ER Experiment, *Science*, 284, 790-793, doi:10.1126/science.284.5415.790.
- Artemyev, A. V., V. Angelopoulos, J. S. Halekas, A. Runov, L. M. Zelenyi, and J. P. McFadden (2017), Mars's magnetotail: Nature's current sheet laboratory, *J. Geophys. Res. Space Physics*, 122, 5404-5417, doi:10.1002/2017JA024078.
- Baumjohann, W., M. Blanc., A. Fedorov, and K.-H. Glassmeier (2010), Current systems in planetary magnetospheres and ionospheres, *Space Sci. Rev.*, 152, 99-134.
- Bertucci, C., F. Duru, N. Edberg, M. Fraenz, C. Martinecz, K. Szego, and O. Vaisberg (2011), The induced magnetospheres of Mars, Venus, and Titan, *Space Science Reviews*, 162(1-4), 113171, doi:10.1007/s11214-011-9845-1.
- Bhattacharyya, D., J. T. Clarke, J.-L. Bertaux, J.-Y. Chaufray, and M. Mayyasi (2015), A strong seasonal dependence in the Martian hydrogen exosphere, *Geophys. Res. Lett.*, 42, 8678-8685, doi:10.1002/2015GL065804.
- Brain, D. A., et al. (2015), The spatial distribution of planetary ion fluxes near Mars observed by MAVEN, *Geophys. Res. Lett.*, 42, 9142-9148, doi:10.1002/2015GL065293.
- Brain, D. A., S. Barabash, S. Bougher, F. Duru, B. Jakosky, and R. Modolo (2017), Solar wind interaction and atmospheric escape, in *The Mars Atmosphere*, edited by B. Haberle et al., Cambridge Univ. Press, Cambridge, doi:10.1017/9781139060172.
- Brecht, S. H., and S. A. Ledvina (2014), The role of the Martian crustal mag-

netic fields in controlling ionospheric loss, *Geophys. Res. Lett.*, 41, 5340-5346, doi:10.1002/2014GL060841.

Chacko, Z., and A. B. Hassam (1997), Steady-state magnetohydrodynamic plasma flow past conducting sphere, *Phys. Plasmas*, 4(8),3031-3039, doi:10.1063/1.872437.

Clarke, J. T., J. L. Bertaux, J. Y. Chaufray, G. R. Gladstone, E. Quemerais, J. K. Wilson, and D. Bhattacharyya (2014), A rapid decrease of the hydrogen corona of Mars, *Geophys. Res. Lett.*, 41, 8013-8020, doi:10.1002/2014GL061803.

Clarke, J. T., et al. (2017), Variability of D and H in the Martian upper atmosphere observed with the MAVEN IUVS echelle channel, *J. Geophys. Res. Space Physics*, 122, 2336-2344, doi:10.1002/2016JA023479.

Cain, J. C., B. B. Ferguson, and D. Mozzoni, An  $n = 90$  internal potential function of the Martian crustal magnetic field, *J. Geophys. Res.*, 108(E2), 5008, doi:10.1029/2000JE001487, 2003.

Connerney, J. E. P., J. Espley, P. Lawton, S. Murphy, J. Odom, R. Oliverson, and D. Sheppard (2015), The MAVEN magnetic field investigation, *Space Sci. Rev.*, 195, 1?35, doi:10.1007/s11214-015-0169-4.

Chaffin, M. S., J.-Y. Chaufray, I. Stewart, F. Montmessin, N. M. Schneider, and J.-L. Bertaux (2014), Unexpected variability of Martian hydrogen escape, *Geophys. Res. Lett.*, 41, 314-320, doi:10.1002/2013GL058578.

DiBraccio, G. A., et al. (2015), Magnetotail dynamics at Mars: Initial MAVEN observations, *Geophys. Res. Lett.*, 42, 8828-8837, doi:10.1002/2015GL065248.

DiBraccio, G. A., et al. (2017), MAVEN observations of tail current sheet flapping at Mars, *J. Geophys. Res. Space Physics*, 122, 4308-4324, doi:10.1002/2016JA023488.

- Dong, Y., X. Fang, D. A. Brain, J. P. McFadden, J. S. Halekas, J. E. Connerney, S. M. Curry, Y. Harada, J. G. Luhmann, and B. M. Jakosky (2015), Strong plume fluxes at Mars observed by MAVEN: An important planetary ion escape channel, *Geophys. Res. Lett.*, 42, 8942-8950, doi:10.1002/2015GL065346.
- Dubinin, E., R. Lundin, W. Riedler, K. Schwingenschuh, J. G. Luhmann, C. T. Russell, and L. H. Brace (1991), Comparison of Observed Plasma and Magnetic-Field Structures in the Wakes of Mars and Venus, *J. Geophys. Res.*, 96, doi:10.1029/91ja01102.
- Dubinin, E., et al., (2009), Ionospheric storms on Mars: Impact of the corotating interaction region, *Geophys. Res. Lett.*, 36, L01105, doi:10.1029/2008GL036559.
- Dubinin, E., and M. Fraenz (2015), Magnetotails of Mars and Venus, in *Magnetotails in the Solar System*, *Geophys. Monogr. Ser.*, vol. 207, edited by A. Keiling, C. M. Jackman, and P. A. Delamere, pp. 43-59, AGU, Washington D. C., doi:10.1002/9781118842324.ch3.
- Edberg, N. J. T., et al. (2009), Plasma boundary variability at Mars as observed by Mars Global Surveyor and Mars Express, *Annales Geophysicae*, 27, 3537-3550.
- Edberg, N. J. T., et al. (2010), Pumping out the atmosphere of Mars through solar wind pressure pulses, *Geophys. Res. Lett.*, 37, L03107, doi:10.1029/2009GL041814.
- Fang, X., Y. Ma, D. Brain, Y. Dong, and R. Lillis (2015), Control of Mars global atmospheric loss by the continuous rotation of the crustal magnetic field: A time-dependent MHD study, *J. Geophys. Res. Space Physics*, 120, 10,926-10,944, doi:10.1002/2015JA021605.
- Fang X. et al., (2017), The Mars crustal magnetic field control of plasma boundary locations and atmospheric loss: MHD prediction and comparison with MAVEN, *J. Geophys.*

Res., 122, doi:10.1002/2016JA023509.

Futaana Y. et al., (2008), Mars Express and Venus Express multi-point observations of geo-effective solar flare events in December 2006, Planetary and Space Science, Volume 56, Issue 6, 873-880, <http://dx.doi.org/10.1016/j.pss.2007.10.014>.

Halekas, J. S., E. R. Taylor, G. Dalton, G. Johnson, D. W. Curtis, J. P. McFadden, D. L. Mitchell, R. P. Lin, and B. M. Jakosky (2015), The solar wind ion analyzer for MAVEN, Space. Sci. Rev., doi:10.1007/s11214-013-0029-z.

Halekas, J. S., et al. (2017), Structure, dynamics, and seasonal variability of the Mars-solar wind interaction: MAVEN solar wind ion Analyzer in-flight performance and science results, J. Geophys. Res. Space Physics, 122, 547-578, doi:10.1002/2016JA023167.

Halekas, J. S. (2017), Seasonal variability of the hydrogen exosphere of Mars, J. Geophys. Res. Planets, 122, 901-911, doi:10.1002/2017JE005306.

Harada, Y., et al. (2015), Magnetic reconnection in the near-Mars magnetotail: MAVEN observations, Geophys. Res. Lett., 42, 8838-8845, doi:10.1002/2015GL065004.

Harada, Y., et al. (2017), Survey of magnetic reconnection signatures in the Martian magnetotail with MAVEN, J. Geophys. Res. Space Physics, 122, 5114-5131, doi:10.1002/2017JA023952.

Jakosky, B. M., et al. (2015a), MAVEN observations of the response of Mars to an interplanetary coronal mass ejection, Science, American Association for the Advancement of Science, 2015, 350 (6261), DOI: 10.1126/science.aad0210.

Jakosky, B. M., et al. (2015b), The Mars Atmosphere and Volatile Evolution (MAVEN) mission, Space Sci. Rev., 195(1-4), 3-48, doi:10.1007/s11214-015-0139-x.

Kallio, E., J.-Y. Chaufray, R. Modolo, D. Snowden, and R. Winglee (2011), Modeling of

Venus, Mars, and Titan, *Space Sci. Rev.*, 162, 267-307, doi:10.1007/s11214-011-9814-8.

Leclercq, L., R. Modolo, F. Leblanc, S. Hess, and M. Mancini (2016), 3D magnetospheric parallel hybrid multi-grid method applied to planet-plasma interactions, *J. Comput. Phys.*, 309, 295-313, doi:10.1016/j.jcp.2016.01.005.

Ledvina, S. A., Y.-J. Ma, and E. Kallio (2008), Modeling and simulating flowing plasmas and related phenomena, *Space Sci. Rev.*, 139, 143-189, doi:10.1007/s11214-008-9384-6.

Lillis, R. J., et al. (2015), Characterizing atmospheric escape from Mars today and through time, with MAVEN, *Space Sci. Rev.*, 195, 357-422, doi:10.1007/s11214-015-0165-8.

Luhmann, J. G., C. T. Russell, K. Schwingenschuh, and Y. Yeroshenko (1991), A comparison of induced magnetotails of planetary bodies: Venus, Mars and Titan, *J. Geophys. Res.*, 96, 11,199-11,208, doi:10.1029/91JA00086.

Luhmann, J. G., C. Dong, Y. Ma, S. M. Curry, D. L. Mitchell, J. R. Espley, J. E. P. Connerney, J. S. Halekas, D. A. Brain, B. M. Jakosky, and C. Mazelle (2015), Implications of MAVEN Mars near-wake measurements and models, *Geophys. Res. Lett.*, 42, doi:10.1002/2015GL066122.

Lundin, R. and S. Barabash (2004), The wakes and magnetotails of Mars and Venus, *Adv. Space Res.*, 33, doi: 10.1016/j.asr.2003.07.054.

Ma, Y., A. F. Nagy, I. V. Sokolov, and K. C. Hansen (2004), Three-dimensional, multi-species, high spatial resolution MHD studies of the solar wind interaction with Mars, *J. Geophys. Res.*, 109, A07211, doi:10.1029/2003JA010367.

Ma, Y., X. Fang, C. T. Russell, A. F. Nagy, G. Toth, J. G. Luhmann, D. A. Brain, and C. Dong (2014), Effects of crustal field rotation on the solar wind plasma interaction with Mars, *Geophys. Res. Lett.*, 41, 6563-6569, doi:10.1002/2014GL060785.

- Ma, Y. J., C. T. Russell, X. Fang, Y. Dong, A. F. Nagy, G. Toth, J. S. Halekas, J. E. P. Connerney, J. R. Espley, P. R. Mahaffy, et al. (2015), MHD model results of solar wind interaction with Mars and comparison with MAVEN plasma observations, *Geophys. Res. Lett.*, 42, 9113-9120, doi:10.1002/2015GL065218.
- Ma, Y. J., et al. (2017), Variations of the Martian plasma environment during the ICME passage on 8 March 2015: A time-dependent MHD study, *J. Geophys. Res. Space Physics*, 122, 1714-1730, doi:10.1002/2016JA023402.
- Masunaga, K., Y. Futaana, G. Stenberg, S. Barabash, T. L. Zhang, A. Fedorov, S. Okano, and N. Terada (2013), Dependence of O<sup>+</sup> escape rate from the Venusian upper atmosphere on IMF directions, *Geophys. Res. Lett.*, 40, 1682-1685, doi:10.1002/grl.50392.
- Mazelle, C., et al. (2004), Bow shock and upstream phenomena at Mars, *Space Sci. Rev.*, 111, 115-181.
- McFadden, J., et al. (2015), The MAVEN Suprathermal and thermal Ion Composition (STATIC) instrument, *Space Sci. Rev.*, 195, 199-256, doi:10.1007/s11214-015-0175-6.
- Modolo, R., G. M. Chanteur, E. Dubinin, and A. P. Matthews (2005), Influence of the solar EUV flux on the Martian plasma environment, *Ann. Geophys.*, 23, 433-444, doi:10.5194/angeo-23-433-2005.
- Modolo, R., G. M. Chanteur, E. Dubinin, and A. P. Matthews (2006), Simulated solar wind plasma interaction with the Martian exosphere: Influence of the solar EUV flux on the bow shock and the magnetic pile-up boundary, *Ann. Geophys.*, 24, 3403-3410, doi:10.5194/angeo-24-3403-2006.
- Modolo, R., G. M. Chanteur, and E. Dubinin (2012), Dynamic Martian magnetosphere: Transient twist induced by a rotation of the IMF, *Geophys. Res. Lett.*, 39, L01106,

doi:10.1029/2011GL049895.

Modolo, R., et al. (2016), Mars-solar wind interaction: LatHyS, an improved parallel 3-D multispecies hybrid model, *J. Geophys. Res. Space Physics*, 121, 6378-6399, doi:10.1002/2015JA022324.

Modolo, R., et al. (2018), The LatHyS database for planetary plasma environment investigations: Overview and a case study of data/model comparisons, *Planetary and Space Science*, <http://dx.doi.org/10.1016/j.pss.2017.02.015>

Nagy, A. et al., (2004). The plasma environment of Mars, *Space Science Reviews*, *Space Science Reviews*, 111, 33-114.

Y. Naor and U. Keshet (2015), Magnetohydrodynamics using path or stream functions, *ApJ*, 810, 152.

Rahmati, A., et al. (2017), MAVEN measured oxygen and hydrogen pickup ions: Probing the Martian exosphere and neutral escape, *J. Geophys. Res. Space Physics*, 122, 3689-3706, doi:10.1002/2016JA023371.

Richer, E., R. Modolo, G. M. Chanteur, S. Hess, and F. Leblanc (2012), A global hybrid model for Mercury's interaction with the solar wind: Case study of the dipole representation, *J. Geophys. Res.*, 117, A10228, doi:10.1029/2012JA017898.

Romanelli, N., D. Gómez, C. Bertucci, and M. Delva (2014), Steady-state magnetohydrodynamic flow around an unmagnetized conducting sphere, *Astrophys. J.*, 789(1), 43.

Romanelli, N., C. Bertucci, D. Gómez, and C. Mazelle (2015), Dependence of the location of the Martian magnetic lobes on the interplanetary magnetic field direction: Observations from Mars Global Surveyor, *J. Geophys. Res. Space Physics*, 120, 7737-7747,

doi:10.1002/2015JA021359.

Romanelli, N., et al. (2016), Proton cyclotron waves occurrence rate upstream from Mars observed by MAVEN: Associated variability of the Martian upper atmosphere, *J. Geophys. Res. Space Physics*, 121, 11,113-11,128, doi:10.1002/2016JA023270.

Romanelli, N., R. Modolo, F. Leblanc, J-Y. Chaufray, A. Martinez, Y. Ma, C. O. Lee, J. G. Luhmann, J. Halekas, D. Brain, G. DiBraccio, J. Espley, J. McFadden, B. Jakosky, Mats Holmström (2018), Responses of the Martian magnetosphere to an interplanetary coronal mass ejection: MAVEN observations and LatHyS results, doi: 10.1029/2018GL077714.

Rong, Z. J., S. Barabash, G. Stenberg, Y. Futaana, T. L. Zhang, W. X. Wan, Y. Wei, and X.-D. Wang (2015), Technique for diagnosing the flapping motion of magnetotail current sheets based on single-point magnetic field analysis, *J. Geophys. Res. Space Physics*, 120, 3462-3474, doi:10.1002/2014JA020973.

Turc, L., D. Fontaine, P. Savoini, and R. Modolo (2015), 3D hybrid simulations of the interaction of a magnetic cloud with a bow shock, *J. Geophys. Res. Space Physics*, 120, 6133-6151, doi:10.1002/2015JA21318.

Vaisberg, O. L. (1992), The solar wind interaction with Mars: A review of results from early Soviet missions to Mars, in *Venus and Mars: Atmospheres, Ionospheres and Solar Wind Interactions*, vol. 66, pp. 311-326, AGU Monograph, Washington, D. C.

Vech, D., G. Stenberg, H. Nilsson, N. J. T. Edberg, A. Opitz, K. Szego, T. Zhang, and Y. Futaana (2016), Statistical features of the global polarity reversal of the Venusian induced magnetosphere in response to the polarity change in interplanetary magnetic field, *J. Geophys. Res. Space Physics*, 121, 3951-3962, doi:10.1002/2015JA021995.

Vignes, D., et al., 2000. The Solar Wind interaction with Mars: locations and shapes of the Bow Shock and the Magnetic Pile-up Boundary from the observations of the MAG/ER experiment onboard Mars Global Surveyor. *Geophysical Research Letters* 27 (1), 49-52.

Winske, D., et al. (2003), Hybrid simulation codes: Past, present and future-A tutorial, in *Space Plasma Simulation Lecture Notes in Physics*, vol. 615, edited by J. Buchner, C. Dum, and M. Scholer, pp. 136-165, Springer, Berlin.

Yamauchi, M., et al. (2015), Seasonal variation of Martian pick-up ions: Evidence of breathing exosphere, *Planet. Space Sci.*, doi:10.1016/j.pss.2015.09.013.

Yeroshenko, Y., W. Riedler, K. Schwingenschuh, J. G. Luhmann, M. Ong, and C. T. Russell (1990), The magnetotail of Mars: Phobos observation, *Geophys. Res. Lett.*, 17, 885-888, doi:10.1029/GL017i006p00885.

Zhang, T. L., J. Du, Y. J. Ma, H. Lammer, W. Baumjohann, C. Wang, and C. T. Russell (2009), Disappearing induced magnetosphere at Venus: Implications for close-in exoplanets, *Geophys. Res. Lett.*, 36, L20203, doi:10.1029/2009GL040515.

Zhang, T.-L., K. Schwingenschuh, C. T. Russell, J. G. Luhmann, H. Rosenbauer, M. I. Verigin, and G. Kotova (1994), The flaring of the Martian magnetotail observed by the Phobos 2 spacecraft, *Geophys. Res. Lett.*, 21, doi:10.1029/94GL01073.

**Table 1.** Estimations of the angular velocity for different regions inside the Martian magnetotail. From left to right, the columns display the region under analysis, the derived angular velocity, the time interval under which the linear fit is performed, the associated  $R^2$  and considered number of points, and the ratio between such angular velocity and that of the IMF rotation.

Region ( $R_M$ )	Angular velocity ( $^\circ/\text{min}$ )	Time (UT)	$R^2$	N	Ratio
0.00 – 1.00	2.1	11 : 18 : 56 – 11 : 23 : 58	0.87	18	10.2 %
1.00 – 1.75	5.9	11 : 18 : 56 – 11 : 23 : 58	0.95	18	28.6 %
1.75 – 2.50	12.8	11 : 17 : 37 – 11 : 21 : 36	0.94	14	62.1 %
2.50 – 3.25	20.1	11 : 17 : 33 – 11 : 20 : 58	0.84	12	97.6 %
IMF	20.6	11 : 17 : 20 – 11 : 20 : 02	0.89	10	-
0.00 – 1.00	-3.3	10 : 44 : 56 – 10 : 47 : 44	0.83	14	9.1%
1.00 – 1.75	-5.6	10 : 44 : 56 – 10 : 47 : 44	0.98	14	15.4%
1.75 – 2.50	-19.0	10 : 44 : 56 – 10 : 46 : 00	0.96	4	52.5 %
2.50 – 3.25	-33.9	10 : 44 : 30 – 10 : 46 : 00	0.85	5	93.6 %
IMF	-36.2	10 : 44 : 02 – 10 : 45 : 16	0.98	5	-
0.00 – 1.00	5.9	10 : 49 : 00 – 10 : 50 : 00	0.89	8	6.1 %
0.00 – 1.00	3.8	10 : 49 : 00 – 10 : 53 : 00	0.95	24	3.9 %
1.00 – 1.75	8.4	10 : 48 : 00 – 10 : 50 : 00	0.98	14	8.7 %
1.00 – 1.75	7.1	10 : 48 : 00 – 10 : 53 : 00	0.98	30	7.3 %
1.75 – 2.50	42.5	10 : 48 : 00 – 10 : 49 : 00	0.99	7	43.8 %
2.50 – 3.25	83.5	10 : 47 : 54 – 10 : 48 : 58	0.86	8	86.0 %
IMF	97.1	10 : 47 : 35 – 10 : 48 : 31	0.85	7	-

**Table 2.** Planetary H<sup>+</sup> and O<sup>+</sup> escape rates through several surfaces.

O <sup>+</sup>	Fluxes (ions/s)
Total escape	$(1.14 \pm 0.08) \times 10^{24}$
$X_{MSO} = -2.4R_M$ escape	$(1.00 \pm 0.07) \times 10^{24}$
⊥ escape	$(1.42 \pm 0.25) \times 10^{23}$
E escape	$(1.15 \pm 0.19) \times 10^{23}$
H <sup>+</sup>	Fluxes (ions/s)
Total escape	$(7.56 \pm 0.16) \times 10^{25}$
$X_{MSO} = -2.4R_M$ escape	$(5.88 \pm 0.08) \times 10^{25}$
⊥ escape	$(1.68 \pm 0.17) \times 10^{25}$
E escape	$(6.55 \pm 1.08) \times 10^{24}$

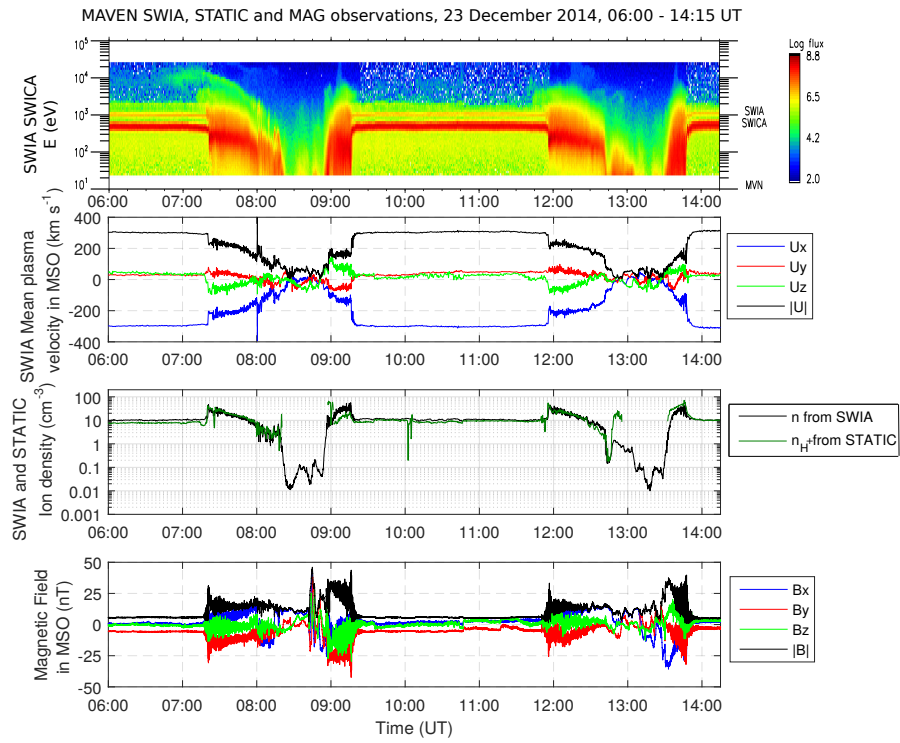


**Figure 1.** MAVEN MAG, SWIA and STATIC observations on 23 December 2014, 06:00 - 14:15 UT. From top to bottom: the SWIA energy spectrogram, the SWIA MSO bulk plasma velocity components and magnitude, the SWIA and STATIC ion densities, and the magnetic field MSO components and magnitude. Black and green curves in the third panel correspond to the mean ion density from SWIA, and the  $H^+$  density from STATIC, respectively.

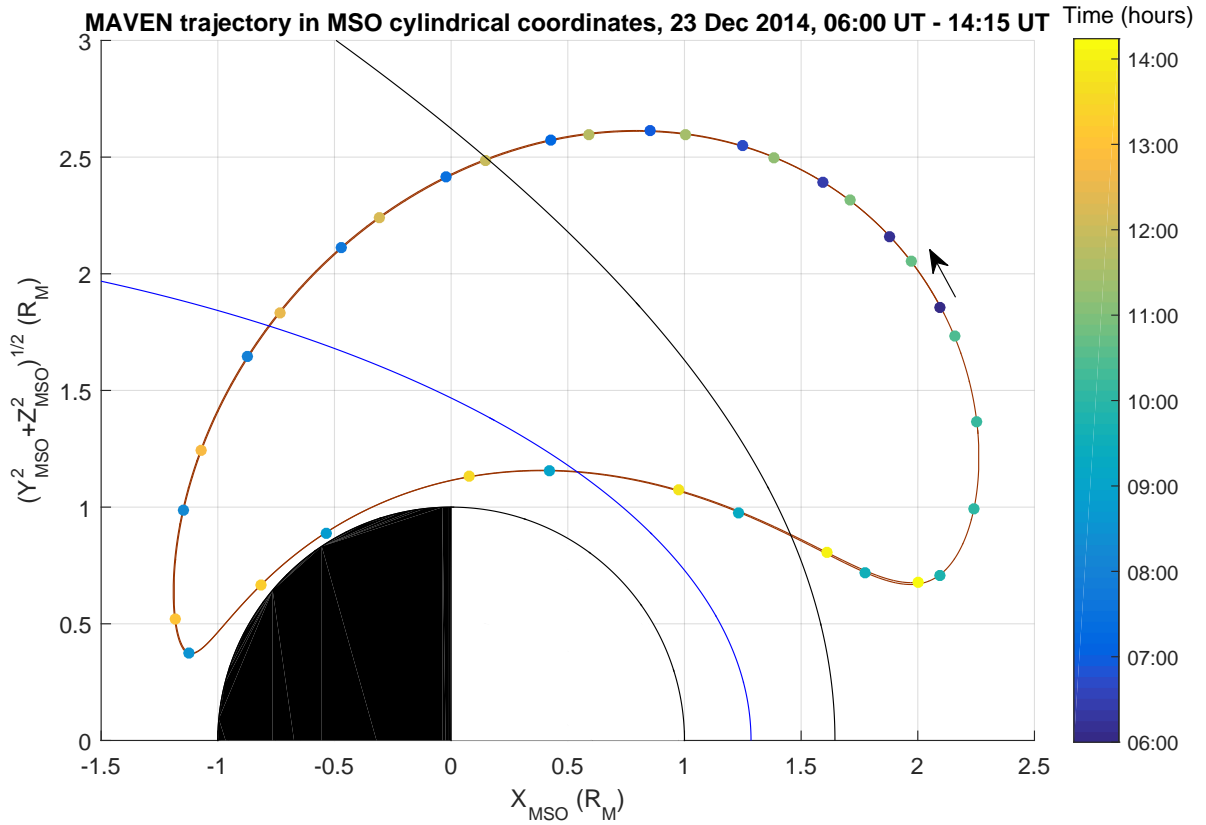


**Figure 2.** MAVEN trajectory in cylindrical MSO coordinates on 23 December 2014, 06:00 - 14:15 UT (in brown). The color-coded points display the position of MAVEN at a particular time, every 15 minutes. Bow shock and magnetic pile up boundary fits [Vignes et al., 2000] are shown in black and blue, respectively.

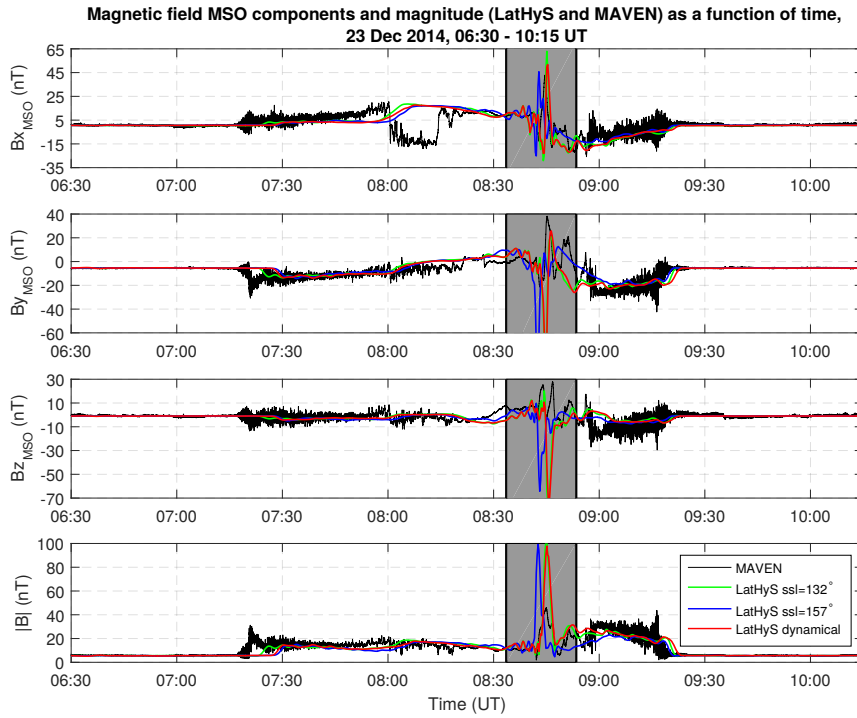


**Figure 3.** LatHyS results and MAVEN measurements of magnetic field MSO components and magnitude for the 23 Dec 2014, 06:30-10:15 UT time interval. Stationary simulation profiles for subsolar longitude at 07:00 UT, at MAVEN’s closest approach, dynamical simulation profiles (ssl varying) and MAVEN MAG observations are shown in blue, green, red and black, respectively. The grey box highlights the time interval where MAVEN’s altitude is 400 km or smaller.

Mean velocity field MSO components and magnitude, and number density (LatHyS and MAVEN),  
23 Dec 2014, 06:30 - 10:15 UT

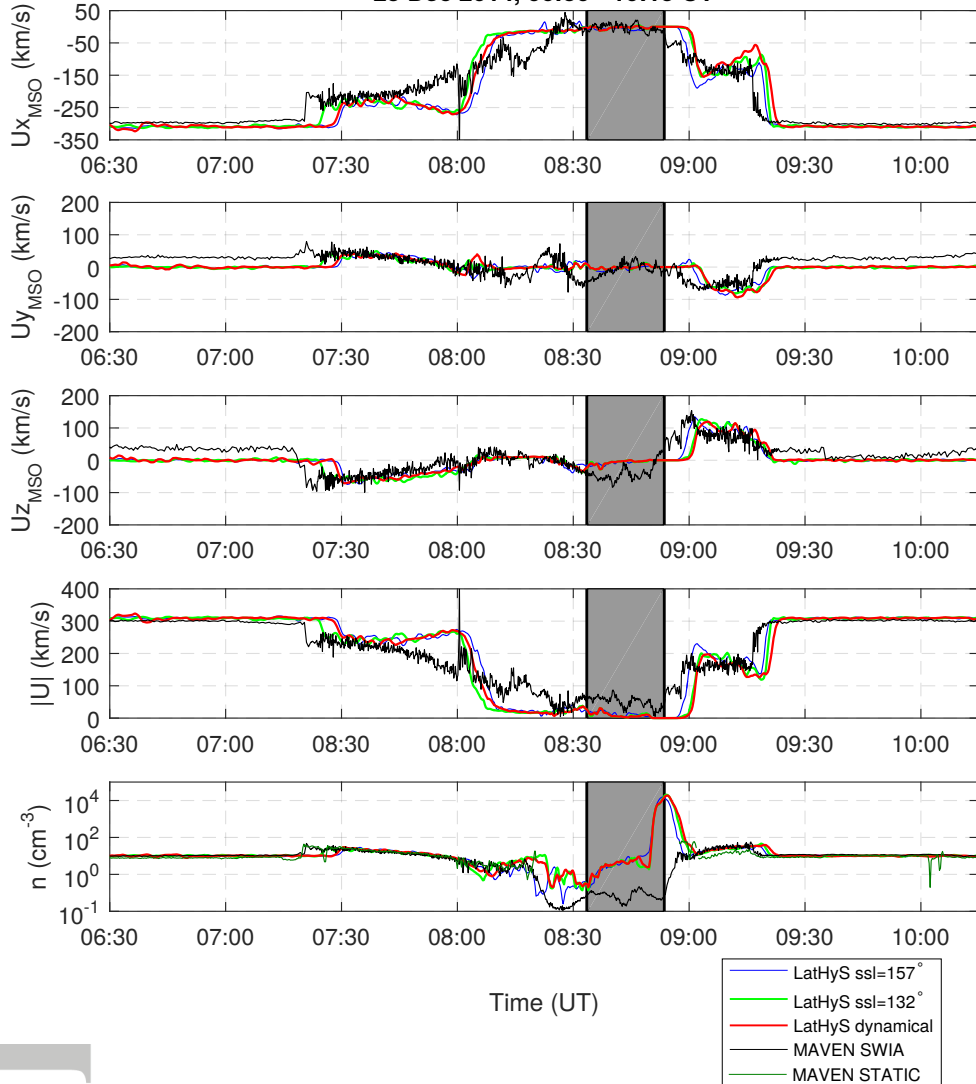


**Figure 4.** LatHyS results and MAVEN measurements of mean velocity field MSO components and magnitude (top to fourth panel) for the 23 Dec 2014, 06:30-10:15 UT time interval. Bottom panel displays LatHyS total ion densities and MAVEN SWIA mean ion density and STATIC  $\text{H}^+$  density as a function of time for the same time interval. Stationary simulation profiles for subsolar longitude at 07:00 UT, at MAVEN's closest approach, dynamical simulation profiles (ssl varying) and MAVEN SWIA observations are shown in blue, light green, red and black, respectively.  $\text{H}^+$  densities from STATIC are shown in green. The grey box highlights the time interval where MAVEN's altitude is 400 km or smaller.

icle

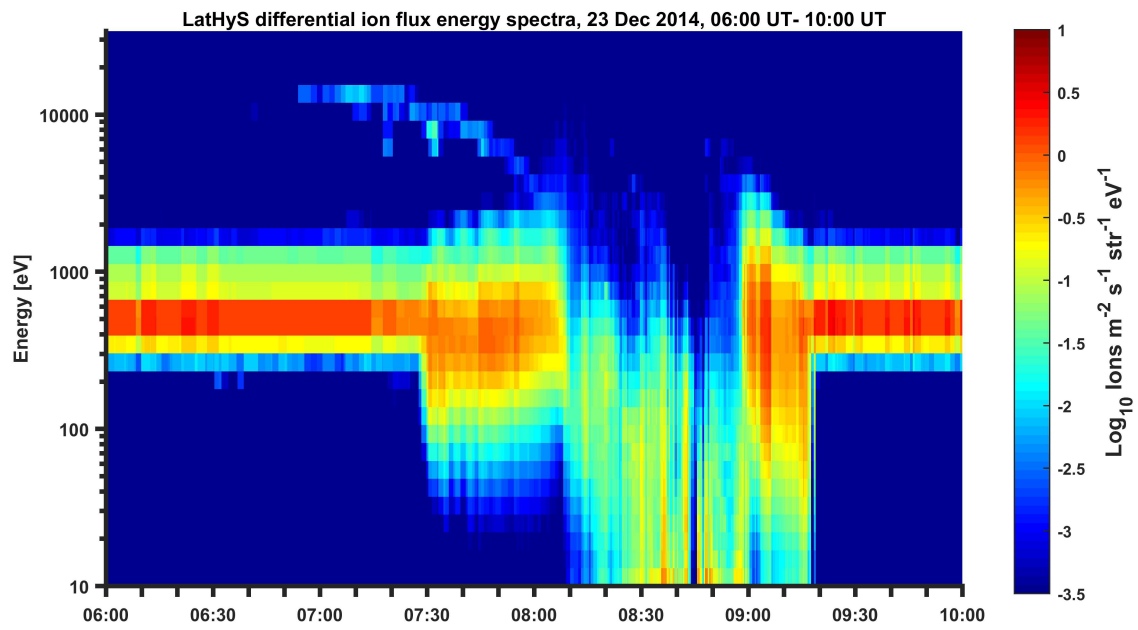


**Figure 5.** LatHyS differential ion flux energy spectra, for conditions in 23 December 2014, between 06:00 and 10:00 UT.

Accepted

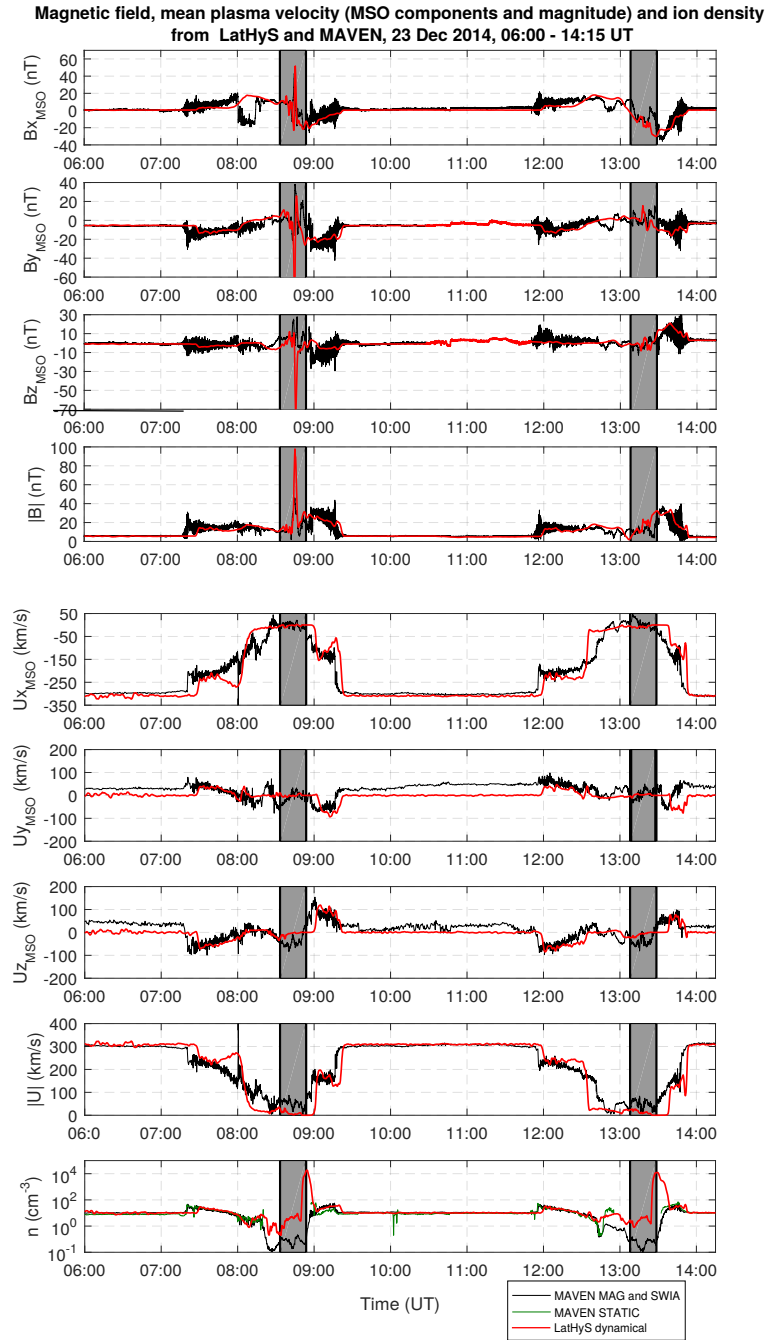


**Figure 6.** LatHyS results and MAVEN observations of magnetic field, mean plasma velocity MSO coordinates and magnitude, and ion density, for the 23 Dec 2014, 06:00-14:15 UT time interval. Dynamical simulation profiles (ssl varying) and MAVEN (MAG and SWIA) observations are shown in red and black, respectively.  $\text{H}^+$  densities from STATIC are shown in green. The grey boxes highlight the time intervals where MAVEN's altitude is 400 km or smaller.

e

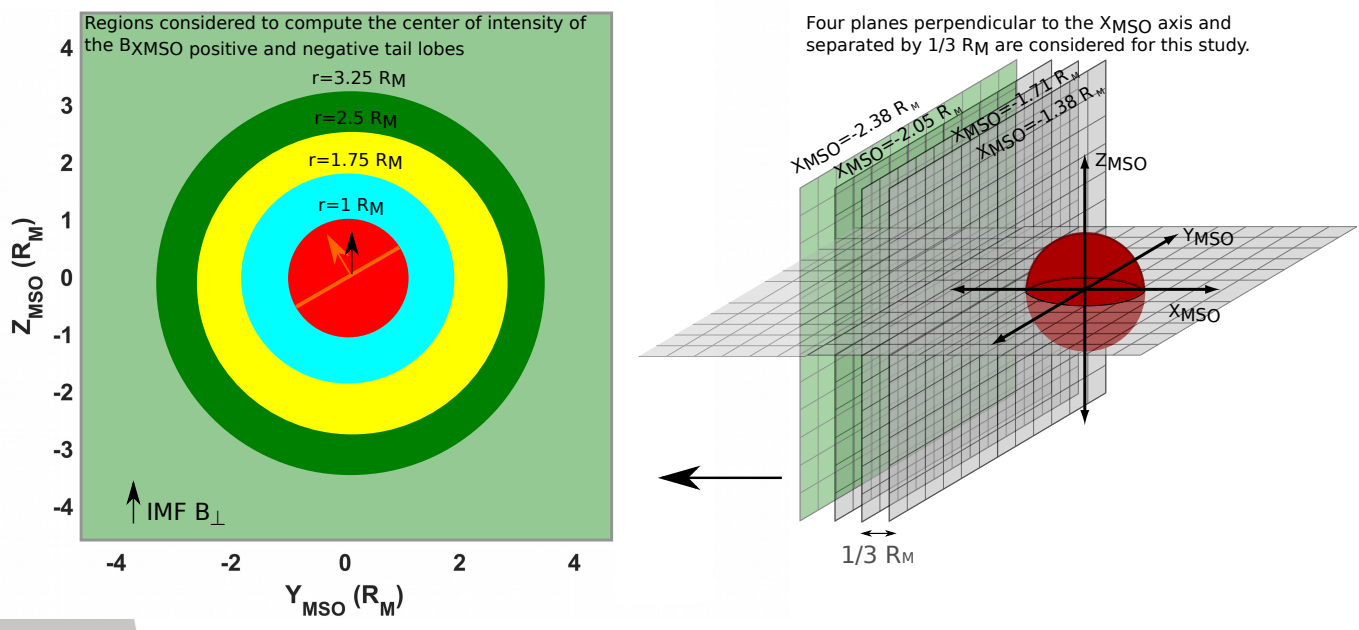


**Figure 7.** Schematic representation of the four circular regions (left panel) and the four planes perpendicular to the  $X_{MSO}$  axis (right panel) considered to characterize the magnetic field orientation inside the Martian magnetotail. The orange vector and segment shown in the left panel represent the normal to the current sheet and the associated performed linear fit. Such current sheet normal estimation, together with the IMF  $B_{\perp}$  and the vector (based on the centers of intensity of the  $B_{xMSO}$  component) associated with each of the 4 circular regions provide 6 estimates of the magnetic field orientation, at each plane.

Accepted

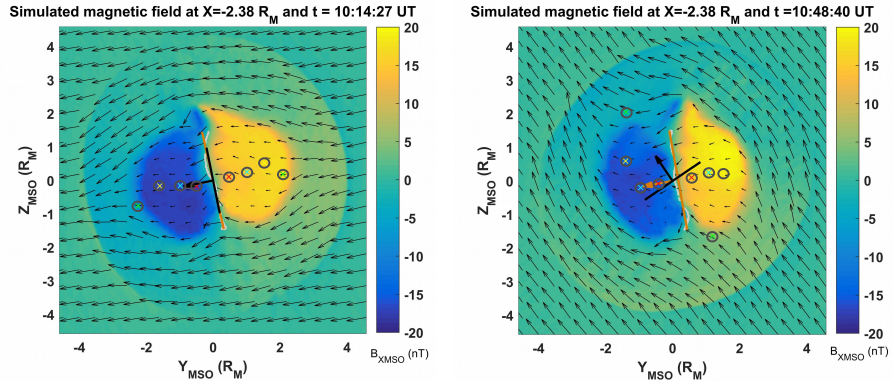


**Figure 8.** Two different states of the Martian magnetotail, according to LatHyS results. Both panels display the  $B_{x_{MSO}}$  component (color-coded) in the  $X_{MSO}=-2.38 R_M$  and the magnetic field perpendicular ( $\mathbf{B}_\perp$ ) to the  $X_{MSO}$  axis (black arrows). Crosses (encircled to facilitate identification) show the location of the centers of intensity of the positive and negative tail lobes (at these planes), for the different circular regions defined in Figure 7. Estimation of the neutral current sheet normal and the local mean IMF  $\mathbf{B}_\perp$  are shown by the thick orange and black arrows.

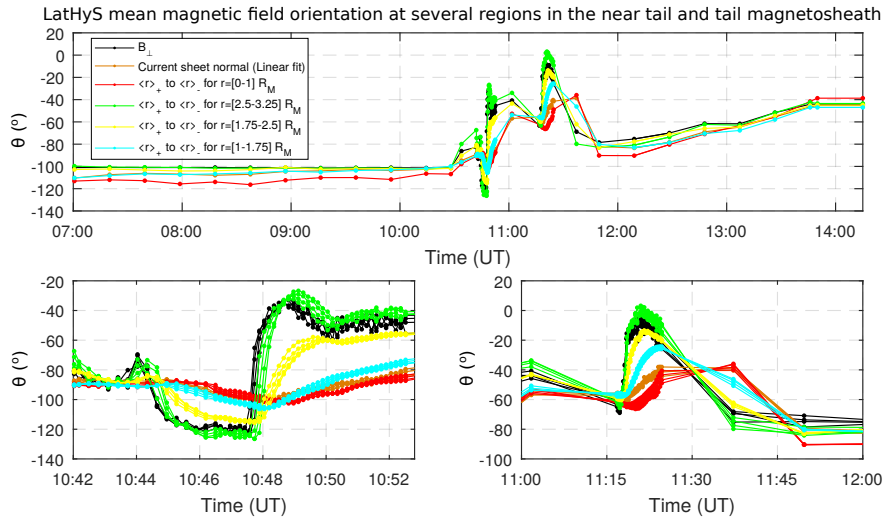


**Figure 9.**  $\theta$  computed from the upstream  $\mathbf{B}_\perp$  (in black) and the vectors defined by the centers of magnetic field intensity in different circular regions and planes (shown in Figure 7), as a function of time. Green, yellow, light blue, and red curves characterize the mean magnetic field orientation over circular rings sampling from the magnetosheath tail up to the inner magnetotail lobes, respectively. The orange curve is associated with the current sheet normal estimate (based on a linear fit). The upper panel shows the set of  $\theta$  curves as a function of time, for 23 Dec 2014, 07:00 - 14:15 UT, for  $X_{MSO} = -2.38 R_M$ . Lower panels show the set of  $\theta$  curves as a function of time during two time subintervals, for all four analyzed planes.

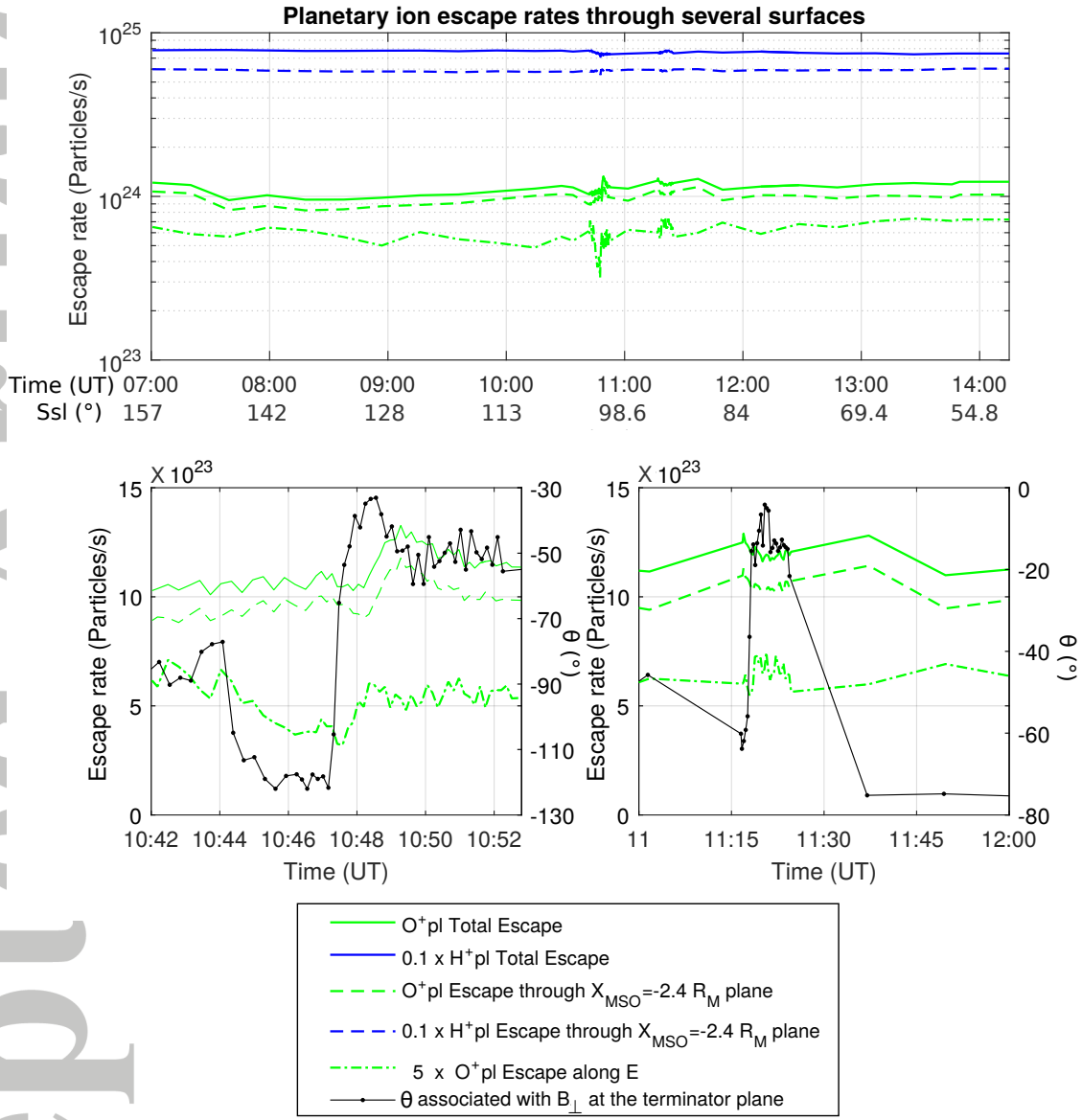


**Figure 10.** Upper panel: LatHyS H<sup>+</sup> and O<sup>+</sup> escape rates through the simulation box, the plane X<sub>M<sub>SO</sub></sub>=-2.4 R<sub>M</sub> and the convective electric field as a function of time. Lower panel: O<sup>+</sup> escape rates (through the simulation box, the plane X<sub>M<sub>SO</sub></sub>=-2.4 R<sub>M</sub> and the convective electric field) and the B<sub>⊥</sub> orientation (θ) at the terminator plane as a function of time.